

1 Introduction

Crustal strain rates are fundamentally important quantities for assessing seismic hazard. This is because the locations where strain is rapidly accumulating are the locations where we can expect strain energy to be released seismically. It is then important to develop and improve upon methods for mapping strain in tectonically active regions because such maps could concievably feed into seismic hazard models such as UCERF3 (Field et al., 2014).

Maps of strain rate can be derived from geodetic measurements of ground displacements, and there are numerous methods for doing so. The classic and simplest way is to assume that the strain rate is constant in time and spatially uniform within subnetworks of the geodetic data. Linear least squares is then used to find the components of the strain rate tensor for each subnetwork (e.g Frank, 1966; Prescott, 1976; Savage et al., 1986; Feigl et al., 1993; Murray and Lisowski, 2000). Several algorithms have been developed to improve upon this procedure for calculating strain. Shen et al. (1996) and Shen et al. (2015) discuss an algorithm where, instead of using the immediately adjacent stations to calculate strain at a position, the strain is computed with a weighted average over the entire network where the weighting is smaller for more distant stations. Another strategy is to fit a set of interpolating basis functions to the velocity field and then compute the strain from the analytical derivative of the interpolant (e.g. Beavan and Haines, 2001; Tape et al., 2009; Sandwell and Wessel, 2016). The aforementioned studies have all been concerned with estimating long term strain rates. Time dependent strain would be useful for studying geophysical processes which occur over timescales of days to years such as slow slip events, postseismic relaxation, or volcanic deformation. Ohtani et al. (2010) describes a Kalman filter based method for computing time dependent strain by fitting a set of basis functions to a time dependent displacement field and enforcing temporal smoothness in the basis function coefficients.

In essence, estimating strain rates is a matter of numerically calculating the spatial derivative of a geodetically observed velocity field. Any method proposed for calculating strain rates must be able to handle two complications: (1) geodetic velocity estimates are noisy and differentiation will only amplify the noise and (2) velocities are not observed on a regular grid, which prevents the use of standard finite difference methods for computing derivatives. In this paper we demonstrate that both of these complications can be elegantly handled with the recently popularized Radial Basis Function-Finite Difference (RBF-FD) method (Wright and Fornberg, 2006).

The RBF-FD method was introduced as an computationally efficient way to solve large scale partial differential equations over irregular, multi-dimensional domains. The RBF-FD method can be thought of as a generalization of the traditional finite difference method, where the node layout is no longer restricted to regular grids. Indeed, the RBF-FD method can be used to estimate derivates of discrete data located at arbitrary scattered positions in multi-dimensional space. The RBF-FD method is particularly appealing because it is algorithmically simple, regardless of the domain shape or node layout, and also because the method has performed well in numerous benchmark tests (Fornberg and Flyer, 2015, and references therein).

In this paper, we do not use the RBF-FD method to solve a partial differential equation, but rather we use it to spatially smooth and differentiate GPS derived velocity data. Our smoothing strategy can be viewed as a low-pass filter for scattered data where the degree of smoothness is controlled by a user specifies cutoff frequency. This can be contrasted with interpolation based smoothing strategies (e.g. Howell et al., 2016) where the resulting interpolant can be largely and unpredictably controlled by the choice of basis function. After spatially smoothing the velocity field we differentiate it with the RBF-FD method to get a strain rate map. We also demonstrate that this procedure can be used to estimate time dependent strain rates. In that case, we first temporally smooth and differentiate GPS displacement time series to get time dependent velocities. We then spatially smooth and differentiate the resulting velocities for each time epoch.

The method proposed in this paper has numerous advantages which set it apart from other methods for computing strain rates. The method is computationally efficient and stable (there is no inversion of an ill-conditioned matrix). There are no hyper parameters or penalty parameters that need to be tuned for each application. As opposed to interpolation strategies such as Beavan and Haines (2001), Tape et al. (2009), or Ohtani et al. (2010), our method assumes that velocities are locally rather than globally continuous, which allows us to easily handle discontinuities resulting from, for example, a creeping fault.

We begin this paper by summarizing the RBF-FD method and explaining how we construct differentiation matrices for scattered data. We then introduce the smoothing strategy, which is applied to the observed geodetic data prior to differentiation. We then provide two real world demonstraitions of our method for calculating strain rates. First we calculate the long term strain rates in Southern California from the CMM3 velocity data set (Shen et al., 2011), and we verify that our results are consistent with other studies. We then calculate time dependent strain rates in Cascadia from the GPS data provided by UNAVCO. In Cascadia, we analyze strain resulting from slow slip events and compare it to the long term tectonic strain accumulation. Slow slip events are found to produce compression in the Olympic Peninsula, which is in addition to the compression resulting from tectonic loading. Further south in Oregon, the slow slip events tend to release the compressional strain that is accumulated tectonically. While similar conclusions have been drawn from fault slip inversions for

slow slip events, it is important to recognize that slip inversion are the product of inverting an ill-conditioned matrix making it difficult to determine whether slip inferences are real or just an artifact of the inversion. The strain rates presented in this paper are more direct observations and can be interpreted with a higher degree of confidence.

2 Method

2.1 Differentiating Scattered Data

In this section we briefly summarize the RBF-FD method and we refer the reader to Wright and Fornberg (2006) or Fornberg and Flyer (2015) for additional details. Consider a set of nodes $\mathbf{x} = \{x_1, \dots, x_N\}$ in \mathbb{R}^d and a corresponding vector $\mathbf{u} = [u(x_1), \dots, u(x_N)]^T$. We want to find a differentiation matrix \mathbf{L} , such that \mathbf{Lu} approximates the linear differential operator \mathcal{L} acting on u at \mathbf{x} . For each node x_i we approximate $\mathcal{L}[u(x)]|_{x=x_i}$ as a weighted sum of $\{u(x_j) : j \in \mathcal{S}^i\}$ where \mathcal{S}^i consist of i and the indices for the $n - 1$ nearest neighboring nodes to x_i . The approximation can be written as

$$\mathcal{L}[u(x)]|_{x=x_i} \approx \sum_{j \in \mathcal{S}^i} L_{ij} u(x_j) \quad (1)$$

where L_{ij} are the weights making up the differentiation matrix \mathbf{L} . We refer to x_i and its $n - 1$ nearest neighbors as the stencil for x_i , and we denote the stencil as $\mathbf{x}^i = \{x_j : j \in \mathcal{S}^i\} = \{x_1^i, \dots, x_n^i\}$. The corresponding weights for each node in \mathbf{x}^i are denoted as $\mathbf{w}^i = \{L_{ij} : j \in \mathcal{S}^i\} = \{w_1^i, \dots, w_n^i\}$. We can then equivalently write eq. (1) as

$$\mathcal{L}[u(x)]|_{x=x_i} \approx \sum_{j=1}^n w_j^i u(x_j^i). \quad (2)$$

Following Fornberg and Flyer (2015), we find the components of \mathbf{w}^i , and thus also of \mathbf{L} , by solving the linear system of equations

$$\begin{bmatrix} \phi(\|x_1^i - x_1^i\|) & \cdots & \phi(\|x_n^i - x_1^i\|) & | & \psi_1(x_1^i) & \cdots & \psi_m(x_1^i) \\ \vdots & & \vdots & | & \vdots & & \vdots \\ \phi(\|x_1^i - x_n^i\|) & \cdots & \phi(\|x_n^i - x_n^i\|) & | & \psi_1(x_n^i) & \cdots & \psi_m(x_n^i) \\ \hline \psi_1(x_1^i) & \cdots & \psi_1(x_n^i) & | & 0 & \cdots & 0 \\ \vdots & & \vdots & | & \vdots & & \vdots \\ \psi_m(x_1^i) & \cdots & \psi_m(x_n^i) & | & 0 & \cdots & 0 \end{bmatrix} \begin{bmatrix} w_1^i \\ w_n^i \\ \vdots \\ \lambda_1 \\ \vdots \\ \lambda_m \end{bmatrix} = \begin{bmatrix} \mathcal{L}[\phi(\|x - x_1^i\|)]|_{x=x_i} \\ \vdots \\ \mathcal{L}[\phi(\|x - x_n^i\|)]|_{x=x_i} \\ \hline \mathcal{L}[\psi_1(x)]|_{x=x_i} \\ \vdots \\ \mathcal{L}[\psi_m(x)]|_{x=x_i} \end{bmatrix} \quad (3)$$

for each stencil. In eq. (3), ϕ is a radial basis function (RBF) which we describe below, $\|\bullet\|$ indicates the L_2 norm, ψ_i are monomial basis functions that span the space of all d -dimensional polynomials with a specified degree p (e.g. $\{1, x, y\}$ for $d = 2$ and $p = 1$), and λ_i are parameters that are estimated along with w_j^i when eq. (3) is inverted but they serve no purpose and can be discarded.

Throughout this paper we use a cubic RBF for ϕ ,

$$\phi(r) = r^3. \quad (4)$$

The cubic RBF is an odd degree polyharmonic spline which has the benefit of being scale invariant and thus there is no scaling parameter that needs to be optimized, unlike for many other common choices of RBFs (e.g. Larsson and Fornberg, 2003). We note that the results presented in this paper remain virtually unchanged when we use other polyharmonic splines for ϕ , which is consistent with the findings of Flyer et al. (2016).

We now elaborate on the stencil size, n , and the polynomial degree, p . We choose p to be equal to the degree of the derivative which we are approximating. This choice is based on the analysis of Flyer et al. (2016) and it ensures that eq. (1) will converge to the true derivative as the distance between nodes decreases. The accuracy of eq. (1) also generally improves with larger values of n , but at the expense of computational costs. We then choose n to be large enough for eq. (1) to converge. For the demonstrations in this paper, we find that $n = 30$ is an appropriate choice. It is worth noting that eq. (3) cannot be inverted when the number of nodes is less than the number of monomial basis functions, m . We then have a lower bound on n which is $n \geq m = \binom{p+d}{d}$.

2.2 RBF-FD Filter

We calculate strain rates by spatially differentiating geodetically observed velocities. In order to differentiate noisy velocity data with the method described in Section 2.1, we must first smooth the data. Existing strategies for smoothing scattered data can be classified as parametric and non-parametric approaches. Parametric approaches involve fitting a set of basis functions to the data, perhaps using least-squares or regularized least-squares (e.g. Fasshauer, 2007). Non-parametric approaches include kernel smoothing (e.g. Hastie and Tibshirani, 1990) and Gaussian process regression (e.g. Rasmussen and Williams, 2006). Kriging is among the better known examples of Gaussian process regression (Matheron, 1963). Many of the wide variety of the existing strategies could surely produce a sufficiently smooth velocity field for us to calculate a coherent strain map. But since the intent of this paper is, in part, to demonstrate the utility of the RBF-FD method in geodesy, we present a smoothing strategy which we refer to as the RBF-FD filter. This method is non-parametric and it offers several features which we find valuable. The RBF-FD filter is computationally efficient and stable, it can be viewed as a low-pass filter with a well defined cutoff frequency, and we can easily specify discontinuities which we do not want to smooth across. In the following discussion of the RBF-FD filter, we seek to find a smoothed solution, \mathbf{u}_{post} , from observed data, \mathbf{u}_{obs} . We constrain \mathbf{u}_{post} with the observation equation

$$\mathbf{u}_{\text{post}} = \mathbf{u}_{\text{obs}} + \boldsymbol{\epsilon}, \quad \boldsymbol{\epsilon} \sim \mathcal{N}(\mathbf{0}, \mathbf{C}_{\text{obs}}), \quad (5)$$

and the prior model

$$\mathbf{u}_{\text{prior}} \sim \mathcal{N}(\mathbf{0}, \mathbf{C}_{\text{prior}}), \quad (6)$$

where $\boldsymbol{\epsilon}$ and $\mathbf{u}_{\text{prior}}$ are considered to be Gaussian processes with zero mean and covariances \mathbf{C}_{obs} and $\mathbf{C}_{\text{prior}}$ respectively. The solution for \mathbf{u}_{post} minimizes the objective function

$$\|\mathbf{u}_{\text{post}} - \mathbf{u}_{\text{obs}}\|_{\mathbf{C}_{\text{obs}}}^2 + \|\mathbf{u}_{\text{post}}\|_{\mathbf{C}_{\text{prior}}}^2 \quad (7)$$

and is itself a Gaussian process with a distribution described by

$$\mathbf{u}_{\text{post}} \sim \mathcal{N}(\bar{\mathbf{u}}_{\text{post}}, \mathbf{C}_{\text{post}}). \quad (8)$$

We use $\bar{\mathbf{u}}_{\text{post}}$ and \mathbf{C}_{post} to denote the mean and covariance of \mathbf{u}_{post} respectively. Using Bayesian linear regression (Tarantola, 2005) these values are found to be

$$\begin{aligned} \bar{\mathbf{u}}_{\text{post}} &= (\mathbf{C}_{\text{obs}}^{-1} + \mathbf{C}_{\text{prior}}^{-1})^{-1} \mathbf{C}_{\text{obs}}^{-1} \mathbf{u}_{\text{obs}} \\ \mathbf{C}_{\text{post}} &= (\mathbf{C}_{\text{obs}}^{-1} + \mathbf{C}_{\text{prior}}^{-1})^{-1}. \end{aligned} \quad (9)$$

\mathbf{C}_{obs} is presumably well known, while $\mathbf{C}_{\text{prior}}$ needs to be chosen based on an understanding of the underlying signal which we are trying to estimate. In Section 2.2.1 we discuss our choice for $\mathbf{C}_{\text{prior}}$ and provide demonstrations with one-dimensional data. The natural extension for $\mathbf{C}_{\text{prior}}$ when dealing with d -dimensional data is discussed in Section 2.2.2.

2.2.1 Filtering in One Dimension

For one-dimensional data we consider a prior which can be stated implicitly as

$$\mathbf{D}_n \mathbf{u}_{\text{prior}} = \mathbf{q}, \quad \mathbf{q} \sim \mathcal{N}(0, \lambda^2), \quad (10)$$

where \mathbf{D}_n is an n 'th order differentiation matrix, and \mathbf{q} is a vector of white noise with constant variance λ^2 . We leave the details of \mathbf{D}_n unspecified for now. The inverse of the prior covariance matrix is

$$\mathbf{C}_{\text{prior}}^{-1} = \lambda^2 \mathbf{D}_n^T \mathbf{D}_n, \quad (11)$$

and the mean and covariance for the posterior are then

$$\begin{aligned} \bar{\mathbf{u}}_{\text{post}} &= (\mathbf{C}_{\text{obs}}^{-1} + \frac{1}{\lambda^2} \mathbf{D}_n^T \mathbf{D}_n)^{-1} \mathbf{C}_{\text{obs}}^{-1} \mathbf{u}_{\text{obs}} \\ \mathbf{C}_{\text{post}} &= (\mathbf{C}_{\text{obs}}^{-1} + \frac{1}{\lambda^2} \mathbf{D}_n^T \mathbf{D}_n)^{-1}. \end{aligned} \quad (12)$$

This solution is closely tied to several well established methods of smoothing. For example, one can immediately recognize eq. (12) as an example of Tikhonov regularization (Tikhonov and Arsenin, 1978). We also note a similarity between eq. (12) and smoothing splines (Wahba, 1990). To see this similarity, recall that a one-dimensional smoothing spline is defined as the function, $f(t)$, which minimizes,

$$\sum_{i=1}^N ((\mathbf{u}_{\text{obs}})_i - f(t_i))^2 + \alpha \int_{t_1}^{t_N} \left(f^{(n)}(t) \right)^2 dt, \quad (13)$$

where $(\mathbf{u}_{\text{obs}})_i$ is an observation at time t_i , N is the number of observations, α is a smoothing parameter, and $f^{(n)}$ denotes the n 'th time derivative of f . In comparison, if we ignore data uncertainties (i.e. $\mathbf{C}_{\text{obs}} = \mathbf{I}$), $\bar{\mathbf{u}}_{\text{post}}$ is the discrete function which minimizes

$$\|\mathbf{u}_{\text{obs}} - \bar{\mathbf{u}}_{\text{post}}\|_2^2 + \frac{1}{\lambda^2} \|\mathbf{D}_n \bar{\mathbf{u}}_{\text{post}}\|_2^2. \quad (14)$$

If the sampling rate for \mathbf{u}_{obs} is constant and the penalty parameters are appropriately chosen then eq. (14) can be recognized as a discretized form of (13). We would thus expect $f(t)$ and $\bar{\mathbf{u}}_{\text{post}}$ to be effectively identical. The key difference between smoothing splines and the method presented here is that the former produces a globally smooth interpolant while we are only requiring local smoothness in our solution. The benefits of imposing local smoothness are discussed in Section 2.3.

We discuss the penalty parameter, λ . One common method for choosing an appropriate penalty parameter is generalized cross-validation (Craven and Wahba, 1979), which yields a smoothed solution with the maximum predictive power. There is merit to using an entirely objective approach such as cross-validation, and this would be appropriate if there is no prior knowledge of the signal's characteristic period. Otherwise, it may be better to choose a penalty parameter that damps out all the high frequency oscillations which are known to be noise.

We demonstrate how λ can be chosen so that frequencies greater than ω_c are attenuated. We make the simplifying assumption that eq. (12) is a linear time-invariant (LTI) filter. In doing so, we assume that \mathbf{u}_{obs} has a constant sampling rate, the data uncertainty is constant and uncorrelated ($\mathbf{C}_{\text{obs}} = \sigma \mathbf{I}$), and $\mathbf{u}_{\text{prior}}$ is periodic. We enforce periodicity in $\mathbf{u}_{\text{prior}}$ by making \mathbf{D}_n the periodic spectral differentiation matrix (e.g. Trefethen, 2000). Under the discrete Fourier transform, \mathbf{D}_n then has the properties

$$\mathcal{F}[\mathbf{D}_n \mathbf{g}]_k = (2\pi i \omega_k)^n \mathcal{F}[\mathbf{g}]_k \quad (15)$$

and

$$\mathcal{F}[\mathbf{D}_n^T \mathbf{g}]_k = (-2\pi i \omega_k)^n \mathcal{F}[\mathbf{g}]_k, \quad (16)$$

where ω_k is the frequency domain variable and \mathbf{g} is an arbitrary vector. With the LTI assumptions, the discrete Fourier transform of $\bar{\mathbf{u}}_{\text{post}}$ is

$$\mathcal{F}[\bar{\mathbf{u}}_{\text{post}}]_k = \frac{\frac{1}{\sigma^2}}{\frac{1}{\sigma^2} + \frac{(2\pi \omega_k)^{2n}}{\lambda^2}} \mathcal{F}[\mathbf{u}_{\text{obs}}]_k. \quad (17)$$

We make the change of variables

$$\lambda^2 = (2\pi \omega_c)^{2n} \sigma^2 \quad (18)$$

which simplifies eq. (17) to

$$\mathcal{F}[\bar{\mathbf{u}}_{\text{post}}]_k = \frac{1}{1 + \left(\frac{\omega_k}{\omega_c}\right)^{2n}} \mathcal{F}[\mathbf{u}_{\text{obs}}]_k. \quad (19)$$

Based on eq. (19), we can recognize the frequency response of eq. (12) to be qualitatively similar to the frequency response for an n 'th order low-pass Butterworth filter with cut-off frequency ω_c . In particular, the frequency response for eq. (12) is flat in the passband and decays log-linearly in the stopband (Figure 1). In the limit as $n \rightarrow \infty$, eq. (12) becomes an ideal low-pass filter which removes all frequencies above ω_c and leaves lower frequencies unaltered.

The above Fourier analysis reveals how eq. (12) will behave under LTI assumptions. For the GPS data considered in this paper, this assumption is not appropriate because neither the data uncertainties nor the sampling rates are constant. When the LTI conditions are not satisfied, it is no longer obvious how eq. (12) behaves or whether it can still be viewed as a low-pass filter with cutoff frequency ω_c .

We explore the behavior of eq. (12) under more general conditions. We continue to substitute λ in eq. (12) with eq. (18), which changes our free parameter to ω_c . Since we are no longer assuming a constant variance, we replace σ^2 in eq. (18) with a characteristic variance, $\bar{\sigma}^2$, which we define as

$$\frac{1}{\sigma^2} = \frac{1}{N} \text{tr}(\mathbf{C}_{\text{obs}}^{-1}), \quad (20)$$

where N is the number of observations. We now write our smoothed solution as

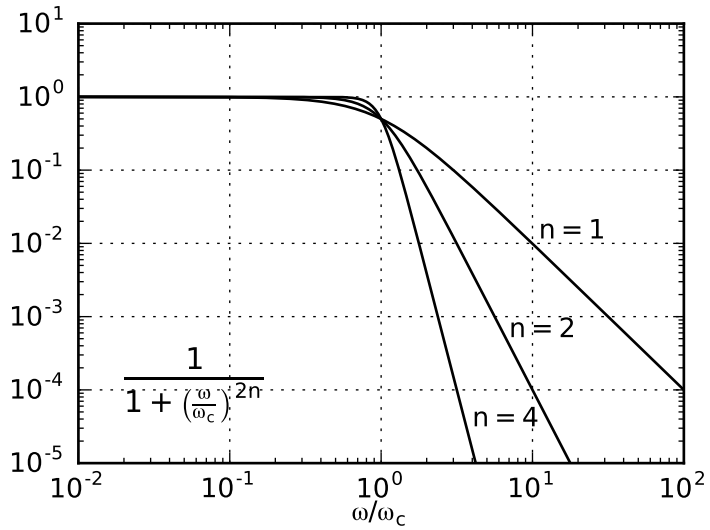


Figure 1: Frequency response of the RBF-FD filter from eq. (19) for different values of n .

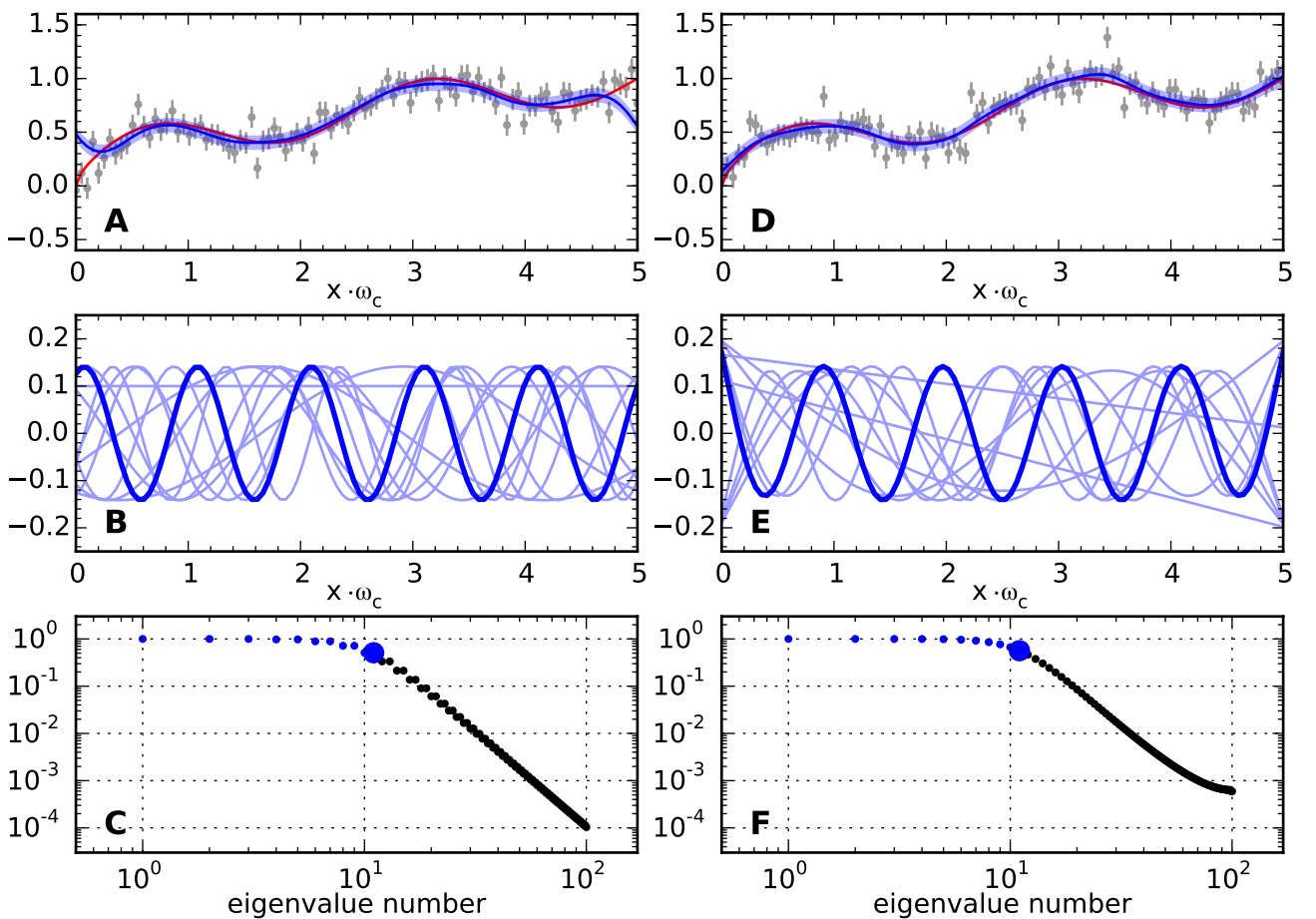


Figure 2: eigenvectors and eigenvalues

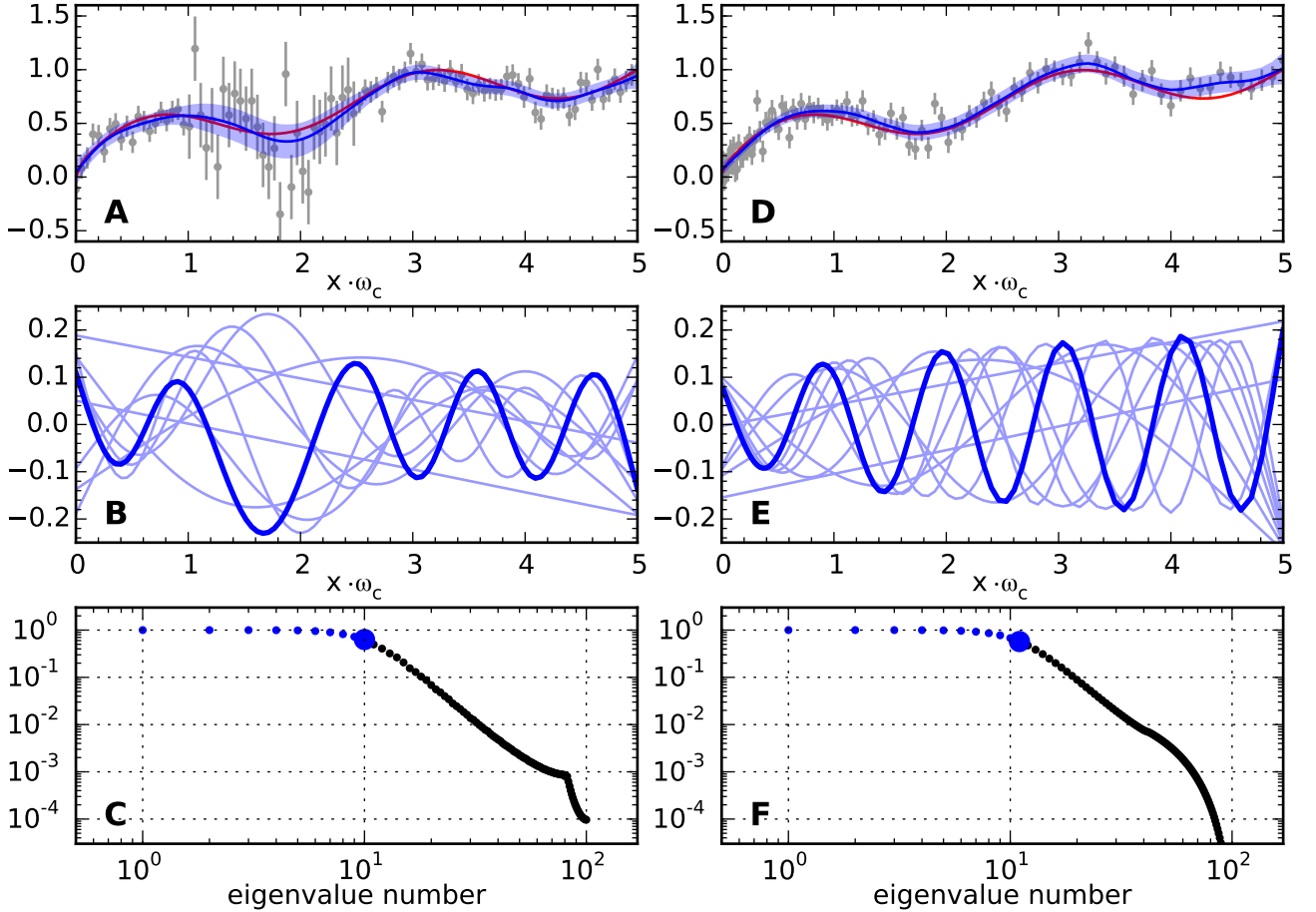


Figure 3: eigenvectors and eigenvalues

$$\begin{aligned}\bar{\mathbf{u}}_{\text{post}} &= (\mathbf{C}_{\text{obs}}^{-1} + \frac{1}{(2\pi\omega_c)^{2n}\bar{\sigma}^2} \mathbf{D}_n^T \mathbf{D}_n)^{-1} \mathbf{C}_{\text{obs}}^{-1} \mathbf{u}_{\text{obs}} \\ \mathbf{C}_{\text{post}} &= (\mathbf{C}_{\text{obs}}^{-1} + \frac{1}{(2\pi\omega_c)^{2n}\bar{\sigma}^2} \mathbf{D}_n^T \mathbf{D}_n)^{-1}.\end{aligned}\quad (21)$$

The behavior of eq. (21) can be revealed by analyzing the eigen decomposition of the matrix mapping \mathbf{u}_{obs} to $\bar{\mathbf{u}}_{\text{post}}$,

$$\mathbf{K} = (\mathbf{C}_{\text{obs}}^{-1} + \frac{1}{(2\pi\omega_c)^{2n}\bar{\sigma}^2} \mathbf{D}_n^T \mathbf{D}_n)^{-1} \mathbf{C}_{\text{obs}}^{-1}. \quad (22)$$

The eigenvalues of \mathbf{K} , $\{s_1, \dots, s_N\}$, are real and bounded between 0 and 1. The eigenvectors, $\{\mathbf{v}_1, \dots, \mathbf{v}_N\}$, are real and, when \mathbf{K} is symmetric (e.g. when $\mathbf{C}_{\text{obs}} = \sigma^2 \mathbf{I}$), form an orthogonal basis set. Each eigenvalue, s_i , describes the amount that \mathbf{v}_i will be shrunk under the mapping \mathbf{K} . The eigenvectors associated with eigenvalues close to 1 can then be interpreted as components which are retained in $\bar{\mathbf{u}}_{\text{post}}$. When the LTI conditions are satisfied, the above Fourier analysis reveals that $\{\mathbf{v}_1, \dots, \mathbf{v}_N\}$ are a set of orthogonal sinusoids and $\{s_1, \dots, s_N\}$ are the corresponding frequency responses from eq. (19) (Figure 2A-C). We show the eigen decomposition of \mathbf{K} under non-LTI conditions where (1) $\mathbf{u}_{\text{prior}}$ is aperiodic (Figure 2D-F), (2) $\mathbf{u}_{\text{prior}}$ is aperiodic and the data uncertainties are not constant (Figure 3A-C), and (3) $\mathbf{u}_{\text{prior}}$ is aperiodic and the data sampling rate is not constant (Figure 3D-F). In all cases, the eigenvectors still resemble sinusoids and the eigenvalues still decay in a manner consistent with the frequency response function in eq. (19), where eq. (19) tells us that the eigenvectors associated with eigenvalues $\geq 1/2$ are sinusoids with frequency $\leq \omega_c$. We can thus conclude that eq. (21) still behaves as a low-pass filter with cutoff frequency ω_c , even when the LTI conditions are not satisfied.

We discuss additional features in the eigenvectors for \mathbf{K} that further illuminate the behavior of eq. (21). When we do not assume periodicity in the underlying signal, the eigenvectors tend to have extreme values at the edges of the domain (Figure 2E). As a result, \mathbf{u}_{post} and \mathbf{C}_{post} also tends to have extreme values at the domain edges. This feature becomes more apparent when $1/\omega_c$ is comparable to the size of the domain. In

Figure 3A-C, we provide a demonstration where the data uncertainties are anomalously high from the time interval 0.2-0.5. The eigenvectors are elongated over this time interval, which is desirable behavior because \mathbf{u}_{post} will not contort to fit dubious data. When the data uncertainty over the time interval 0.2-0.5 is increased to infinity, \mathbf{u}_{post} converges to a solution which is not significantly different from that shown in Figure 3A. One could then surmise that the RBF-FD filter can be used for interpolation by treating interpolation points as data with infinite uncertainty. Lastly, when \mathbf{u}_{obs} does not have a constant sampling rate, the eigenvectors maintain a constant frequency of ω_c and their amplitudes decrease where the data concentration is higher (Figure 3E). The lower amplitude in the eigenvectors reflects the fact that the solution is more tightly constrained.

2.2.2 Filtering in Higher Dimensions

We expand our discussion to smoothing data which is observed in d -dimensional space. We now consider the prior model

$$\mathbf{L}_n \mathbf{u}_{\text{prior}} = \mathbf{q}, \quad \mathbf{q} \sim \mathcal{N}(0, (2\pi\omega_c)^{2n}\bar{\sigma}^2) \quad (23)$$

where \mathbf{L}_n is a differentiation matrix which approximates the operation

$$\sum_{i=1}^d \frac{\partial^n}{\partial x_i^n} \quad (24)$$

and n is an even integer. The variance chosen for \mathbf{q} was motivated by the analysis in Section 2.2.1. The mean and covariance of \mathbf{u}_{post} is now described by

$$\begin{aligned} \bar{\mathbf{u}}_{\text{post}} &= (\mathbf{C}_{\text{obs}}^{-1} + \frac{1}{(2\pi\omega_c)^{2n}\bar{\sigma}^2} \mathbf{L}_n^T \mathbf{L}_n)^{-1} \mathbf{C}_{\text{obs}}^{-1} \mathbf{u}_{\text{obs}} \\ \mathbf{C}_{\text{post}} &= (\mathbf{C}_{\text{obs}}^{-1} + \frac{1}{(2\pi\omega_c)^{2n}\bar{\sigma}^2} \mathbf{L}_n^T \mathbf{L}_n)^{-1}. \end{aligned} \quad (25)$$

If we again assume that the observation are regularly spaced, have constant variance, and \mathbf{L}_n is the corresponding spectral differentiation matrix, then the d -dimensional discrete Fourier transform of $\bar{\mathbf{u}}_{\text{post}}$ is

$$\mathcal{F}[\bar{\mathbf{u}}_{\text{post}}]_k = \frac{1}{1 + \left(\sum_{i=1}^d \left(\frac{\omega_{i,k}}{\omega_c}\right)^n\right)^2} \mathcal{F}[\mathbf{u}_{\text{obs}}]_k. \quad (26)$$

The frequency response for eq. (25) can once again be recognized as a low-pass filter with cutoff frequency ω_c . In the limit as $n \rightarrow \infty$, the frequency response becomes a d -dimensional box which is zero for all the frequency tuples $(\omega_{1,k}, \dots, \omega_{d,k})$ which have at least one component whose magnitude is greater than ω_c .

In general, \mathbf{L}_n can be constructed with the RBF-FD scheme described in Section 2.1, which allows us to use eq. (25) to smooth irregularly spaced data. When that data are irregularly spaced, or if any of the above mentioned idealized conditions are not satisfied, eq. (25) exhibits the same behavior noted in Section 2.2.1. In particular, it can be verified through eigen decomposition that the frequency content of $\bar{\mathbf{u}}_{\text{post}}$ is consistent with ω_c , regardless of the spacing or uncertainty of \mathbf{u}_{obs} .

2.3 Accounting for Known Discontinuities

The RBF-FD filter from Section 2.2 and the RBF-FD differentiation scheme from Section 2.1 can both account for known discontinuities from, for example, a creeping fault segment. When using the RBF-FD scheme to estimate the strain rate from a velocity field, it is important not to use stencils that include stations which are on opposite sides of a creeping fault segment. Doing so could result in estimated strain rates which are erroneously high. The stencils should thus be constructed so that no two stations within a stencil form an edge which intersects the trace of the creeping segment. We also construct stencils in this manner when forming the differentiation matrix \mathbf{L}_n from eq. (25). By doing so, the RBF-FD filter will not produce a solution that is incorrectly tapered across a known discontinuity.

We elaborate on the statistical implications for how we handle discontinuities for the RBF-FD filter. When \mathbf{L}_n is constructed with the RBF-FD scheme, we can interpret $\mathbf{u}_{\text{prior}}$ as a Gaussian Markov random field (e.g. Rue and Held, 2005). That is to say, if $\mathbf{u}_{\text{prior}}$ is known at all stations except for x_i , the probability distribution function for $\mathbf{u}_{\text{prior}}$ at x_i will only depend on $\mathbf{u}_{\text{prior}}$ at stations within a neighborhood of x_i . The neighborhood consists of all stations which share a stencil with x_i . Our strategy for handling discontinuities thus imposes conditional independence between $\mathbf{u}_{\text{prior}}$ at any two stations which form an edge that intersects the trace of a creeping fault segment.

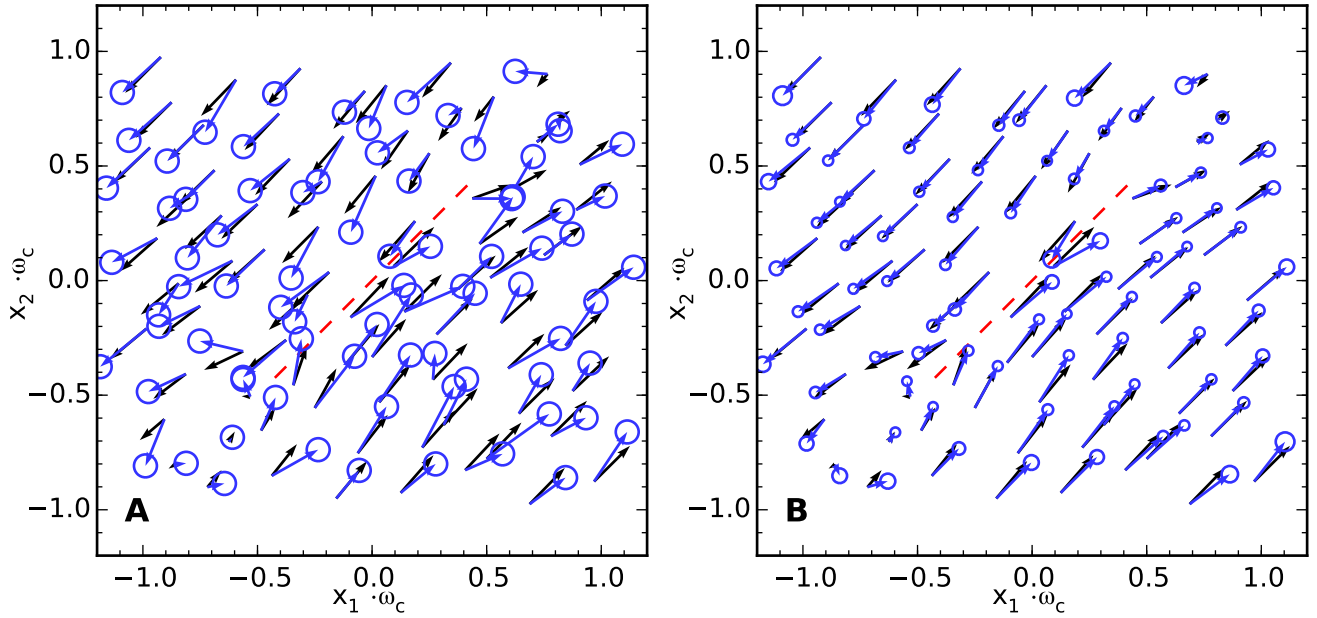


Figure 4: eigenvectors and eigenvalues

We demonstrate smoothing synthetic, scattered, two-dimensional vector data where there is a known discontinuity which we do not want to smooth across (Figure 4). The synthetic data is intended to simulate GPS velocities near a creeping fault segment. We generate the synthetic data with the elastic dislocation solution provided by Okada (1992) and obscure the underlying signal with white noise. We smooth both directional components of the synthetic data independently with eq. (25). Figure 4A and 4B show the observed, \mathbf{u}_{obs} , and smoothed, \mathbf{u}_{post} , data compared to the true signal. As noted in Section 2.2.1, \mathbf{u}_{post} tends to have the highest uncertainty at the domain edges, and that is where \mathbf{u}_{post} does the poorest job at recovering the original signal. Nonetheless, almost every smoothed datum in \mathbf{u}_{post} is an improvement over \mathbf{u}_{obs} at representing the underlying signal.

2.4 Numerical Notes

Do not compute the inverse for \mathbf{u}_{post} !

This is well conditioned and lends itself well to iterative matrix solvers

The posterior covariance matrix is generally dense. If memory does not permit the covariance matrix to be computed and one is only interested in the the data uncertainties then one can find the uncertainties by...

The posterior uncertainty does not account for error in \mathbf{L}

3 Applications

3.1 Strain Rate in Southern California

We provide a demonstration in which we estimate the long term strain rates in southern California from the SCEC crustal motion map (CMM4)(Shen et al., 2011). The crustal motion map provides an estimate of time-averaged horizontal velocities at over one thousand irregularly spaced points in sothern California. The CMM4 is constrained by three decades of geodetic data and velocities have been corrected for coseismic and postseismic motions. We independently smooth easting and northing components of the CMM4 velocities with the RBF-FD filter using a cutoff frequency $\omega_c = 0.01 \text{ km}^{-1}$. We do not smooth the velocities across the creeping segment of the San Andreas Fault (SAF), which extends from Parkfield to Hollister. We show a comparison between the CMM4 velocities and smoothed velocities as supplementary material. We then differentiate the smoothed velocities with the RBF-FD scheme to find the velocity gradient and strain rates. The estimated strain rates, complete with propagated uncertainties, are shown in Figure 5, and it accurately illuminates well known features. The strain map highlights the SAF and shows that the orientation of maximum shear strain runs parallel with the SAF strike (Lisowski et al., 1991). Shear strain rates along the SAF are particularly high ($0.3 - 0.4$ micro-strain per year) in the Salton Trough and at the ends of the creeping segment. We can observe N-S contraction in the Los Angeles basin at a rate of $0.1 - 0.2$ micro-strain per year (Shen et al., 1996; Argus

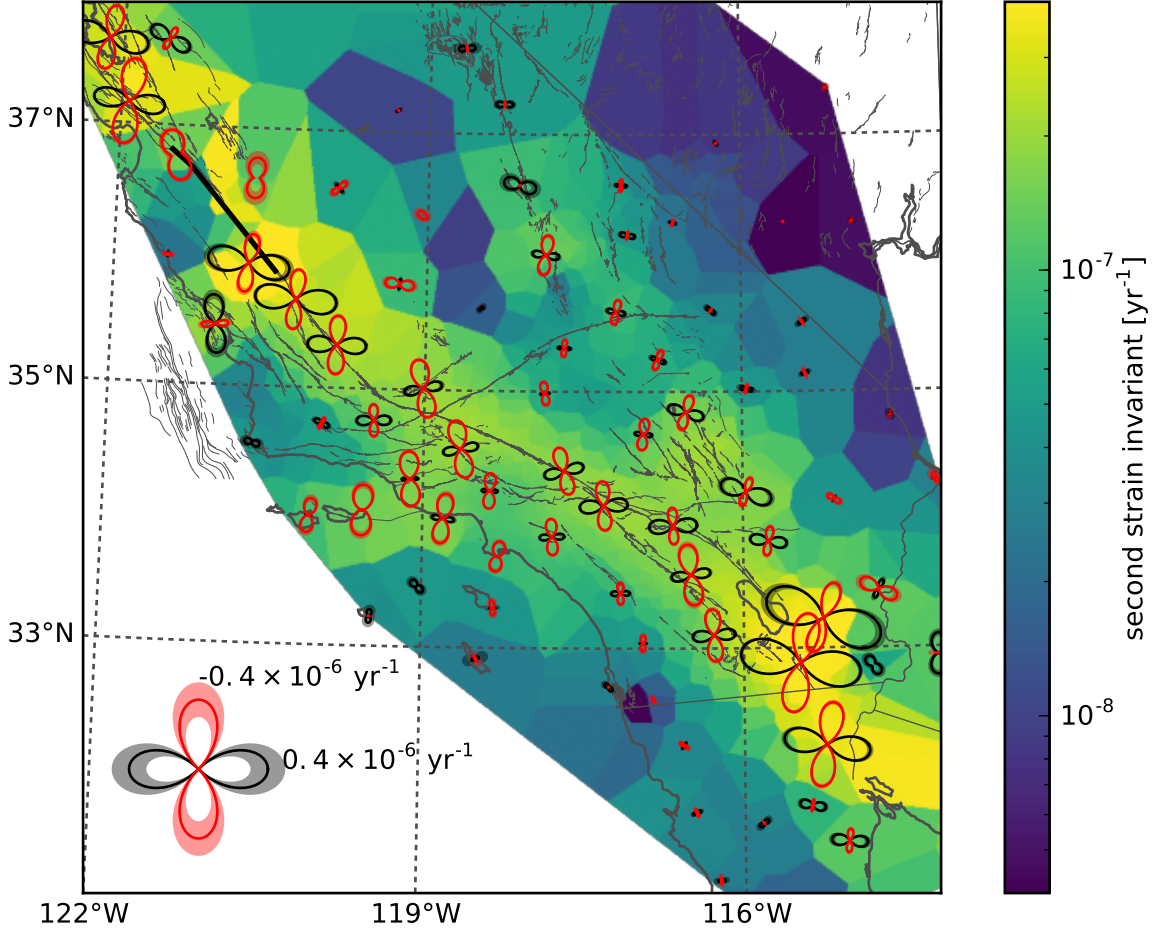


Figure 5: Southern California strain map

et al., 1999, 2005). We also observe a diffuse band of shear strain along the Eastern California shear zone (cite). These results are also consistent with the strain map by Shen et al. (2015), which was derived from the same data set.

The uncertainties on our strain estimates are shown as semi-transparent fields around the strain glyphs, and it may appear that our inferred strain rates are overly confident. In particular, the uncertainties on the estimated strain rates in Nevada are surprisingly low, given the sparse station coverage. There are two sources of error which could potentially result in underestimated uncertainties: (1) we could have chosen a cutoff frequency that is too low for the geophysical signal that we are interested in and (2) the data coverage may be too sparse for the differentiation matrices to be accurate numerical approximations of the corresponding differential operators. The former is a well recognized bias inherent in any smoothing method (Hastie and Tibshirani, 1990), and we address the latter here. Ideally, we would want the average distance between adjacent stations to be $< 1/\omega_c$. Such a dense coverage would ensure that the differentiation matrix used to estimate the velocity gradient is sufficiently accurate. In this demonstration, the data spacing in Nevada is comparable to $1/\omega_c = 100$ km. One remedy for the sparse coverage is to use the RBF-FD filter to interpolate the smoothed solution onto a finer grid of points and then find the velocity gradient of the denser smoothed data set. As suggested in Section 2.2, the RBF-FD filter can be used for interpolation by treating the interpolation points as data with infinite uncertainty. Doing so will increase the accuracy of velocity gradient estimates, but at the expense of increased computational cost. Figure 6A shows a map of estimated strain rates where we improved the accuracy of velocity gradient estimate by interpolating the smoothed velocities on a grid with a ~ 5 km spacing. The inferred strain rates at points along the SAF, where the coverage is sufficiently dense, do not appear to be significantly improved by the added interpolation points. The uncertainties on the strain rates in Nevada are much higher, and likely more appropriate, when we included the interpolation points.

In Figure 6B, we highlight the creeping segment of the SAF, which is a notably problematic area when trying to estimate strain rates in southern California (e.g. Sandwell and Wessel, 2016). We find that the strain rate is greatest at the two ends of the creeping segment, near Parkfield and Hollister. We are also able to resolve a quadrant pattern of extension and compression at the ends of the creeping segment. This strain pattern is consistent with what would be expected from an elastic dislocation model, giving us confidence that the inferred

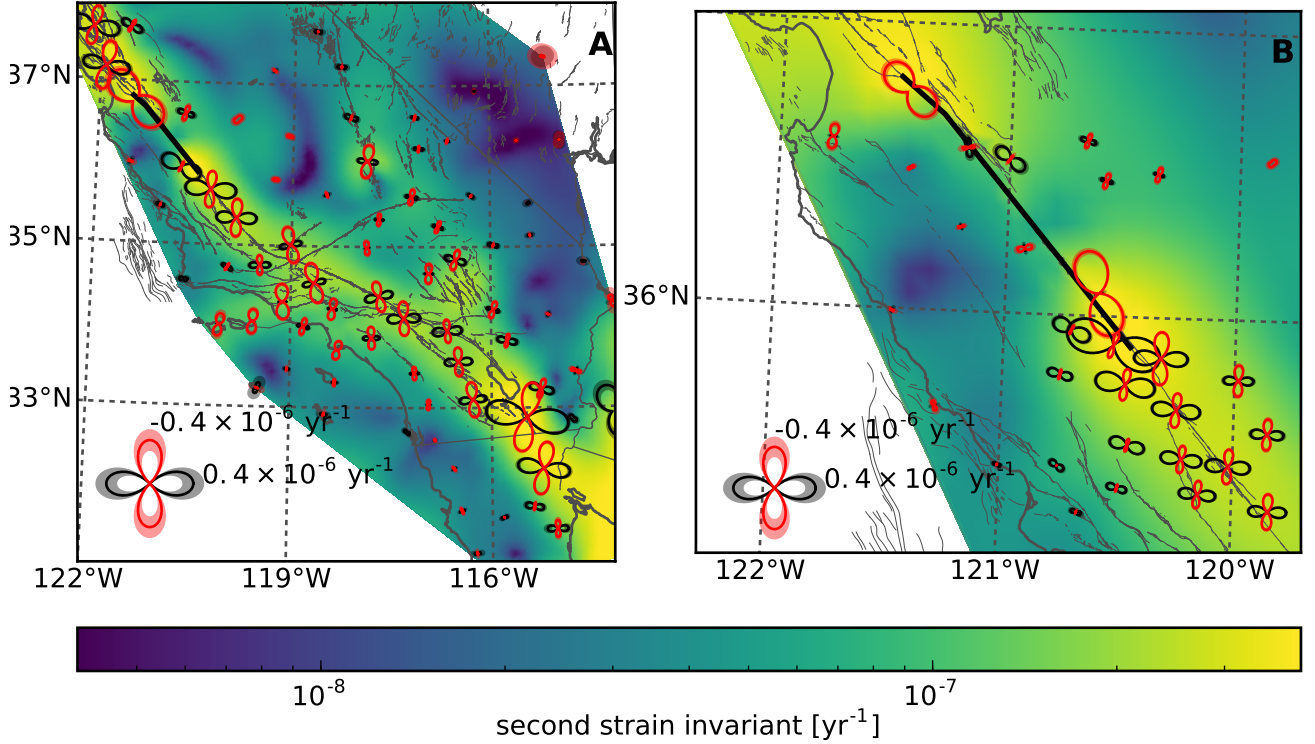


Figure 6: Southern California strain map

strain rates are accurate.

3.2 Time Dependent Strain Rate in Cascadia

4 Discussion and Conclusion

References

- Argus, D. F., Heflin, M. B., Donnellan, A., Webb, F. H., Dong, D., Hurst, K. J., Jefferson, D. C., Lyzenga, G. A., Watkins, M. M., and Zumberge, J. F. (1999). Shortening and thickening of metropolitan Los Angeles measured and inferred by using geodesy. *Geology*, 27(8):703–706.
- Argus, D. F., Heflin, M. B., Peltzer, G., Crampé, F., and Webb, F. H. (2005). Interseismic strain accumulation and anthropogenic motion in metropolitan Los Angeles. *Journal of Geophysical Research B: Solid Earth*, 110(B04401):1–26.
- Beavan, J. and Haines, J. (2001). Contemporary horizontal velocity and strain rate fields of the Pacific-Australian plate boundary zone through New Zealand. *Journal of Geophysical Research*, 106(B1):741–770.
- Craven, P. and Wahba, G. (1979). Smoothing noisy data with spline functions: estimating the correct degree of smoothing by the method of generalized cross-validation. *Numerische Mathematik*, 40:377–403.
- Fasshauer, G. E. (2007). *Meshfree Approximation Method with Matlab*. World Scientific Publishing Co., Singapore.
- Feigl, K. L., Agnew, D. C., Bock, Y., and Dong, D. (1993). Space Geodetic Measurement of Crustal Deformation in Central and Southern California, 1984–1992. *Journal of Geophysical Research*, 98(B12):21 677–21 712.
- Field, E. H., Arrowsmith, R. J., Biasi, G. P., Bird, P., Dawson, T. E., Felzer, K. R., Jackson, D. D., Johnson, K. M., Jordan, T. H., Madden, C., Michael, A. J., Milner, K. R., Page, M. T., Parsons, T., Powers, P. M., Shaw, B. E., Thatcher, W. R., Weldon, R. J., and Zeng, Y. (2014). Uniform California Earthquake Rupture

Forecast, version 3 (UCERF3) -The time-independent model. *Bulletin of the Seismological Society of America*, 104(3):1122–1180.

Flyer, N., Fornberg, B., Bayona, V., and Barnett, G. A. (2016). On the role of polynomials in RBF-FD approximations: I. Interpolation and accuracy. *Journal of Computational Physics*, 321:21–38.

Fornberg, B. and Flyer, N. (2015). *A Primer on Radial Basis Functions with Applications to the Geosciences*. Society for Industrial and Applied Mathematics, Philadelphia.

Frank, C. F. (1966). Deduction of earth strains from survey data. *Bulletin of the Seismological Society of America*, 56(1):35–42.

Hastie, T. J. and Tibshirani, R. J. (1990). *Generalized Additive Models*, volume 1. Chapman and Hall, London.

Howell, S., Smith-Konter, B., Frazer, N., Tong, X., and Sandwell, D. (2016). The vertical fingerprint of earthquake cycle loading in southern California. *Nature Geoscience*, (June).

Larsson, E. and Fornberg, B. (2003). A numerical study of some radial basis function based solution methods for elliptic PDEs. *Computers and Mathematics with Applications*, 46:891–902.

Lisowski, M., Savage, J. C., and Prescott, W. H. (1991). The velocity field along the San Andreas Fault in central and southern California. *Journal of Geophysical Research*, 96(B5):8369.

Matheron, G. (1963). Principles of geostatistics. *Economic Geology*, 58(8):1246–1266.

Murray, M. H. and Lisowski, M. (2000). Strain accumulation along the Cascadia subduction zone in western Washington. *Geophysical Research Letters*, 27(22):3631–3634.

Ohtani, R., McGuire, J. J., and Segall, P. (2010). Network strain filter: A new tool for monitoring and detecting transient deformation signals in GPS arrays. *Journal of Geophysical Research: Solid Earth*, 115(12):1–17.

Okada, Y. (1992). Internal deformation due to shear and tensile faults in a half space. *Bulletin of the Seismological Society of America*, 82(2):1018–1040.

Prescott, W. H. (1976). An extension of Frank’s method for obtaining crustal shear strains from survey data. *Bulletin of the Seismological Society of America*, 66(6):1847–1853.

Rasmussen, C. E. and Williams, C. K. I. (2006). *Gaussian processes for machine learning*. The MIT Press.

Rue, H. and Held, L. (2005). *Gaussian Markov Random Fields: Theory and Applications*. Chapman and Hall, Boca Raton.

Sandwell, D. T. and Wessel, P. (2016). Interpolation of 2-D vector data using constraints from elasticity. *Geophysical Research Letters*, pages 1–7.

Savage, J. C., Prescott, W. H., and Gu, G. (1986). Strain accumulation in southern California, 1973–1984. *Journal of Geophysical Research*, 91(B7):7455–7473.

Shen, Z., Wang, M., Zeng, Y., and Wang, F. (2015). Optimal Interpolation of Spatially Discretized Geodetic Data. *Bulletin of the Seismological Society of America*, 105(4):2117–2127.

Shen, Z. K., Jackson, D. D., Ge, B. X., and Bob, X. G. (1996). Crustal deformation across and beyond the Los Angeles basin from geodetic measurements. *Journal of Geophysical Research*, 101(B12):27927–27957.

Shen, Z. K., King, R. W., Agnew, D. C., Wang, M., Herring, T. A., Dong, D., and Fang, P. (2011). A unified analysis of crustal motion in Southern California, 1970–2004: The SCEC crustal motion map. *Journal of Geophysical Research: Solid Earth*, 116(11):1–19.

Tape, C., Musé, P., Simons, M., Dong, D., and Webb, F. (2009). Multiscale estimation of GPS velocity fields. *Geophysical Journal International*, 179(2):945–971.

Tarantola, A. (2005). *Inverse problem theory and methods for model parameter estimation*. SIAM.

Tikhonov, A. N. and Arsenin, V. Y. (1978). Solutions of Ill-Posed Problems . by A . N . Tikhonov ; V . Y . Arsenin Review by : John B . Bell Stable URL : <http://www.jstor.org/stable/2006360> . *American Mathematical Society*, 32(144):1320–1322.

Trefethen, L. N. (2000). *Spectral Methods in Matlab*. SIAM.

Wahba, G. (1990). *Spline Models for Observational Data*. Philadelphia.

Wright, G. B. and Fornberg, B. (2006). Scattered node compact finite difference-type formulas generated from radial basis functions. *Journal of Computational Physics*, 212(1):99–123.